Instance segmentation and statistical analysis of large-field-of-view X-ray computed tomography data of fiber weave structures

Sabrina Weber[1], Benedikt Boos[2], Kevin Chen[2], Matthias Weber[1], Philipp Rieder[1], Volker Schmidt[1], Andreas Gebhard[2], Martin Gurka[2]

[1]Institut für Stochastik, Universität Ulm, Ulm, Germany, e-mail: sabrina.weber@uni-ulm.de

[2]Leibniz-Institut für Verbundwerkstoffe GmbH, Kaiserslautern, Germany, e-mail: benedikt.boos@ivw.uni-kl.de

Abstract
We present methods for the geometric characterization of hierarchical 3D microstructures of continuously carbon fiber reinforced composites made from stacked woven textile preforms, using X-ray CT and statistical image analysis. As the representative volume of these composites is rather large (in-plane side length > 20 mm) and, simultaneously, contains very small details (< 10 µm), we propose to divide the characterization procedure into three steps, considering (1) single rovings, (2) single weave layers, and (3) full laminates. In this paper, we focus on the geometry of single rovings and a single weave layer. Special emphasis is put on deviations from idealized shapes, including deformation of the commonly assumed elliptical cross section of single rovings, which results from the interaction between the undulating orthogonal rovings. We show that roving cross sections exhibit periodic changes in shape corresponding to their position in the weave structure. Using a mathematical modeling approach, we quantify the variability between rovings.

Keywords: X-ray phase contrast computed tomography, instance segmentation, U-net, carbon fiber reinforced composite, statistical image analysis, weave structure

1 Introduction

Carbon fiber reinforced polymers (CFRPs) provide exceptional mechanical properties by combining specifically arranged strong and stiff fibers or woven structures thereof with a ductile polymer matrix. The mechanical performance of CFRPs is largely governed by the underlying fiber architecture, which follows a hierarchical organization from individual fibers to rovings, textile layers, and laminate. This microstructure, as designed for the specific application, together with random variations therein, determines the resulting mechanical behavior of the final composite, as well as the processing properties during its manufacturing. As an example, the permeability of the semi finished textile controls the resin flow during the liquid molding processes through the textiles pore structure, comprising microscale pores between individual fibers and mesoscale pores between adjacent rovings [1]. To better understand the influence of the fiber structure on both mechanical and processing properties, data-driven in-silico methods provide benefits over expensive experimental setups. However, these methods rely on the availability of realistic digital models of the 3D microstructure of CFRPs, which in turn require detailed 3D characterization – typically based on X-ray computed tomography (CT).

Despite many advances in data acquisition, e.g. µ-CT [2], phase-contrast [3–5] or dark-field imaging [5–7], and also data analysis [8–11], quantitative 3D microstructure evaluation is still a challenge for highly inhomogeneous fiber reinforced polymer composites, especially for composites with carbon fibers [12]. Large-field-of-view data sets with single-fiber resolution are needed to produce realistic representative volume elements, including sufficient statistical variation, resulting in repeated scanning with long acquisition times [13]. In addition to being expensive in costs and time, it puts high demands on the stability of the experimental setup and on the radiation resistance of the investigated sample. Therefore, for the development of data-driven in-silico methods, parametrized stochastic 3D models of the microstructure are a viable alternative, providing the geometry input for spatially resolved numerical modeling and simulation of processing and material properties [14].

To obtain a realistic stochastic 3D microstructure model of a woven textile structure, a prior detailed analysis of the microstructure is essential, with particular emphasis on the deviation from the ideal shape of the intended fiber architecture. This is important because idealized geometry models have been shown to overestimate stiffness and strength due to their neglect of irregularities in roving trajectories [15]. Additionally, the divergence of cross sections of the fiber bundles from assumed perfect shapes is of interest [16]. To analyze these variations from an idealized geometry, accurate instance-wise segmentation is required. Initially, a phase-wise segmentation of warp, weft and matrix can be performed, employing structural tensor techniques or deep learning approaches such as U-nets [8, 10]. Identification and separation of individual rovings remain challenging due to frequent contact and overlapping areas. Thus, some post-processing is necessary to obtain an instance-wise segmentation. For example, a watershed algorithm can be combined with estimated roving trajectories [17].

Based on instance-wise segmentation, the roving trajectories and cross sections can be analyzed. For textile modeling, commonly considered parameters include the weave pattern, roving spacing, and a simplified description of the shape of the rovings cross sections. Typically, roving cross sections are assumed to be ellipses, power ellipses, or lenticular shapes [16, 18–20]. However, these shapes do not accurately describe asymmetric cross sections, which is why independent variables are introduced for the height of the upper and lower half of the cross section. Then, appropriate transition functions allow for smooth transitions

between symmetric and asymmetric cross sections; see [21]. Some modeling tools provide additional functionalities, for example, simulating roving widening in crossover points [22], accounting for cross section deformations based on the roving-surface intersections [23, 24] or allowing user-specified changes of different roving segments [22–24]. These developments emphasize the need for a thorough understanding of the trajectories and cross sectional shapes of the rovings. In particular, cross sections should not be assumed to be constant, but instead vary along each roving [21, 25]. To quantify these variations, we developed a method for analyzing various aspects of cross sectional shapes. For this, we individually analyze the cross sections of each roving at a large number of discrete positions along the roving. Then we compute the descriptors of size, asymmetry, and orientation of each cross section. Tracking these parameters along each roving reveals quantifiable periodic patterns.
In the present paper, we apply this method to a single layer of textile preform with continuously woven carbon fibers. The analysis of a single layer isolates the intrinsic geometric variability of individual rovings from distortions from inter-layer nesting or compaction present in multilayer laminates. In addition to analyzing the shapes of the rovings as described above, we analyze the variability in the weave pattern in terms of roving distance and orientation. Finally, we discuss possible causes, implications, and relevance for textile models of the measured variability in CFRPs on different scales.

2 Methods

For the analysis of variability in the weave structure and roving cross sections, a single layer of textile preform embedded in an epoxy matrix was considered. The sample was imaged via phase-contrast X-ray µ-CT, and the resulting data was segmented using a 2.5D U-net.

2.1 Specimens

A single-ply laminate, consisting of a 2/2 twill G-weave (5 yarns/cm in both warp and weft; each yarn comprising 3000 carbon fibers of 7 µm diameter) embedded in epoxy resin was analyzed. Warp and weft define the main fiber directions in the laminate. Warp yarns run along the fabric and are pre-tensioned during weaving, whereas weft yarns run orthogonally to the warp yarns. The specimen of size $27 \times 27 \times 2$ mm^3 was prepared by punching out a fabric section and embedding it in resin with minimal residual stress to preserve the original microstructure. Embedding also prevented the release of electrically conductive carbon fibers during scanning. A photograph of the embedded specimen is shown in Figure 1.

Figure 1: Embedded cutout of a 2/2 twill G-weave; the arrow indicates the 0° warp direction.

2.2 Data acquisition

X-ray CT scanning was performed with a Zeiss Versa 520 in phase-contrast configuration and a voxel size of 7.0 µm (see Figure 2). Using a detector with 2024×2024 pixels, 2001 projections were recorded. This resulted in a field of view (FOV) of $14.168 \times 14.168 \times 14.007$ mm^3. The accelerating voltage was 80 kV and the electrical power was 7 W. The projections were acquired with an exposure time of 4.5 s per projection, at which the average intensity of the first projection was approximately 5000, resulting in a total scanning time of approximately 150 minutes. Note that the specimens were oriented so that both warp and weft were positioned at a 45° angle relative to the rotation axis. This avoided the issue of 0° and 90° fibers attenuating X-rays differently, thereby providing adequate contrast.

2.3 Preprocessing and segmentation of image data

The measured 3D image data was preprocessed to enable quantitative analysis of the weave structure and rovings. Therefore, intensity normalization was performed on the gray value histogram to improve contrast and suppress outliers. More precisely, the gray values of the voxels were linearly scaled and clamped between the 5 %- and 95 %-percentiles. The image was then segmented into three phases, i.e., matrix, warp and weft, using a 2.5D U-net with depth 5, patch size $64 \times 64 \times 3$ and an initial filter count of 64 as implemented in Dragonfly software [26]. Therefore, slicing was performed in the through-plane direction to facilitate differentiation between the roving orientations. Note that, hand labeling of only two slices was sufficient to generate the ground-truth data for the neural network training. To improve phase-wise segmentation, holes were filled within the segmented masks.
Formally, the resulting phase-wise segmentation can be defined by the mapping $I_\mathrm{P}\colon W \to \{0,1,2\}$, where $W \subset \mathbb{Z}^3$ denotes the

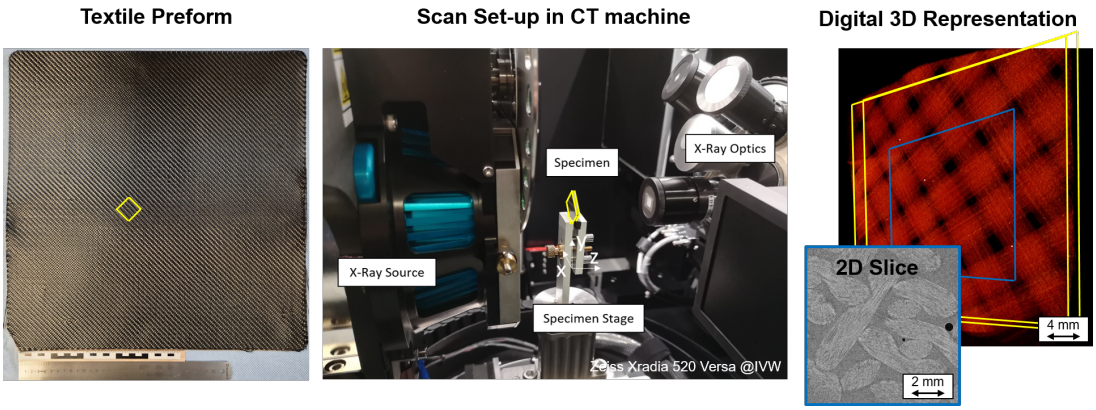

Figure 2: From textile preform (left), to X-ray CT scan (center) and digital 3D representation(right).

sampling window with $\mathbb{Z} = \{\dots, -1, 0, 1, \dots\}$, and

$$I_{\mathrm{P}}(v) = \begin{cases} 1, & \text{if } v \text{ belongs to weft,} \\ 2, & \text{if } v \text{ belongs to warp,} \\ 0, & \text{else,} \end{cases}$$

for each $v \in W$. To analyze individual rovings, an instance segmentation into n rovings $R_1, \dots, R_n \subset W$ was computed for some $n \in \mathbb{N} = \{1, 2, \dots\}$, which is formally given by the mapping $I_{\mathrm{R}} \colon W \to \{0, 1, \dots, n\}$, where

$$I_{\mathrm{R}}(v) = \begin{cases} i, & \text{if } v \text{ belongs to } R_i, \\ 0, & \text{else,} \end{cases}$$

for each $v \in W$. To obtain the instance segmentation, a morphological erosion with radius $r = 5.0$ was applied followed by a dilation with radius $r = 4.9$ [27]. The connected components of the resulting image constitute the desired instance segmentation. In addition, a slight curvature was detected in the data, which justified another post-processing step to correct it. Therefore, the center of gravity, i.e., the center point of the laminate in through-plane direction, was determined at each in-plane position where at least one voxel across all slices is assigned to a roving. A cubic polynomial then was fitted using the least squares method, shifting all centers of gravity to the 0 line in through-plane direction. Using this cubic polynomial, the through-plane position of the whole 3D image is corrected at each in-plane position, so that the curvature, remaining from sample preparation, then is eliminated.

2.4 Statistical image analysis

Geometrical descriptors for cross sections. The geometry of each roving is essentially defined by its trajectory and its cross sections. As cross sections vary along the trajectory of a roving, a detailed analysis and description of cross sections at a sufficiently large number of positions is an important part of understanding the geometry of the roving [18, 28]. Based on the previously obtained instance segmentation, the cross sections of each roving were computed and statistically analyzed. The cross sections of an exemplarily selected roving at different longitudinal positions along the roving (denoted as y-positions) are shown in Figure 3. Note that, as expected, the cross sections differ for each of these positions. In the following, we introduce various geometrical descriptors to quantify these variations. For each $i \in \{1, \dots n\}$, we denote the cross section of the roving R_i at the j-th y-position by $C_{i,j} \subset R_i$, where $j \in \{1, \dots, m_i\}$, and $m_i \in \mathbb{N}$ denotes the number of y-positions considered for R_i. Note that for cross sectional descriptors a local coordinate system is considered where y points along the length of the roving, z is the global through-plane direction and x is orthogonal to both; see Figure 3.

To more precisely specify the position of the cross section $C_{i,j}$, its **centroid** $c(C_{i,j}) = (x_{i,j}, y_{i,j}, z_{i,j}) \in C_{i,j}$ is determined. The sequence $c(C_{i,1}), \dots c(C_{i,m_i})$ of the cross section centroids may be considered as the centerline of the roving R_i, thus representing its undulation and trajectories within the weave structure. In particular, the z-coordinates of the centroids change when the roving passes underneath or over an orthogonal roving.

In addition to its position, the size of $C_{i,j}$ is characterized by its **area** $a(C_{i,j})$, which is computed using the point-count method [29]. As basic descriptors of the cross sectional shape, the **orientation** and **length of its major and minor axes** are determined, where the minor and major axes are computed by fitting a moment-equivalent ellipse to $C_{i,j}$, denoting their lengths by $l_1(C_{i,j})$ and $l_2(C_{i,j})$, respectively. The orientation $o(C_{i,j}) \in [-90°, 90°)$ of $C_{i,j}$ is given by the angle between the major axis and the z-axis of the coordinate system of $C_{i,j}$. More details on the computation of the moment-equivalent ellipse can be found in [30].

For a precise characterization of the shape, various idealized cross sectional shapes, such as ellipses, power ellipses, and lenticular shapes, are commonly assumed [18–20, 31, 32]. However, as visualized in Figure 3, the cross sections can exhibit an asymmetric

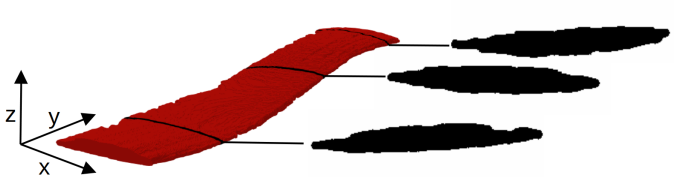

Figure 3: Cross sections along the roving shown at different y-positions.

and more complex shape where one side is relatively flat. In this paper, **skewness** is used to quantify this behavior. Therefore, the vertical distribution of the number of voxels per row within $C_{i,j}$ is considered. For this, $C_{i,j}$ is first aligned horizontally using $o(C_{i,j})$. Then, the number of voxels in each row along the z-direction is determined. The k-the row is denoted by r_k ($k \in \{1,\dots,N_{i,j}\}$), where the number of rows that contain voxels belonging to $C_{i,j}$ is denoted by $N_{i,j}$. For r_k, the computed normalized number of voxels $p_k(C_{i,j})$ is obtained by dividing the number of voxels in the row by the number of voxels belonging to $C_{i,j}$. Thus, the family $\{p_k(C_{i,j})\}_{k=1}^{N_{i,j}}$ defines a discrete, one-dimensional probability distribution of the number of voxels per row along the z-direction. The mean position in the z-direction is then given by $\mu_{i,j} = \sum_{k=1}^{N_{i,j}} r_k(C_{i,j}) p_k(C_{i,j})$. To quantify the asymmetry of $C_{i,j}$ in the z-direction, the skewness is defined as

$$\gamma(C_{i,j}) = \frac{\sum_{k=1}^{N_{i,j}} (r_k(C_{i,j}) - \mu_{i,j})^3}{\sum_{k=1}^{N_{i,j}} (r_k(C_{i,j}) - \mu_{i,j})^2}.$$

For a perfect elliptical cross section $C_{i,j}$, i.e., a symmetric distribution of the normalized number of voxels $p_k(C_{i,j})$, the skewness $\gamma(C_{i,j})$ is 0. Thus, the skewness of this distribution indicates how strongly and in which direction the cross section of the roving deviates from a symmetric shape. For negative skewness, i.e., $\gamma(C_{i,j}) < 0$, the roving cross section is flatter at the bottom, while positive skewness, i.e., $\gamma(C_{i,j}) > 0$, indicates that it is flatter at the top.

Descriptor evolution along rovings. The shape of the cross sections of the rovings changes along its length [25, 33, 34], see Figure 3. As will be shown in Section 3.2, the z-position $z_{i,j}$ of the centroid $c(C_{i,j})$, the skewness $\gamma(C_{i,j})$, and the orientation $o(C_{i,j})$ of the cross sections of R_i exhibit periodic patterns along the y-positions. We will model these patterns using sinusoidal curves $g : \mathbb{R} \to \mathbb{R}$, given by

$$g(y) = A\sin(2\pi f y + \phi) + C, \tag{1}$$

for $y \in \mathbb{R}$, where $A, f, \phi, C \in \mathbb{R}$ denote the amplitude, frequency, phase shift, and offset of the sinusoidal curve. These parameters have to be calibrated for each roving R_i, $(i = 1,\dots,n)$ and each considered descriptor d, where d represents the z-position, the skewness or the orientation of the cross section of a roving. For this purpose, we minimized the mean squared error (MSE) between $g(y_{i,j})$ and the corresponding descriptor value $d_{i,j}$ at position $y_{i,j}$ $(j = 1,\dots,m_i)$. More precisely, the values $(A_{i,d}, f_{i,d}, \phi_{i,d}, C_{i,d}) \in \mathbb{R}^4$ were determined by

$$(A_{i,d}, f_{i,d}, \phi_{i,d}, C_{i,d}) = \underset{(A_{i,d}, f_{i,d}, \phi_{i,d}, C_{i,d}) \in \mathbb{R}^4}{\operatorname{argmin}} \frac{1}{m_i} \sum_{(y_{i,j}, d_{i,j}) \in M} (g(y_{i,j}) - d_{i,j})^2, \tag{2}$$

where $M = (y_{i,j}, d_{i,j})$ is a set of pairs consisting of the position along the roving $y_{i,j}$, $(j \in \{1,\dots,m_i\})$ and the corresponding descriptor value $d_{i,j} \in \mathbb{R}$. The computation of the parameters was performed using *curvefit* of the python package *scikit-learn* [35].

Analysis of the weave structure. In addition to individual rovings, the weave structure was analyzed. For this analysis, we ignored the extent of the weave in the z-direction and focussed on the in-plane geometry. Thus, for each roving R_i ($i \in \{1,\dots,n\}$), we computed its 2D projection $I_i : W \to \{1,0\}$ given by

$$I_i(x,y) = \begin{cases} 1, & \text{if at least one voxel at position} (x,y,z) \text{ for some through-plane coordinate belongs to } R_i \\ 0, & \text{else.} \end{cases}$$

Then, I_i was used to extract the width and approximate centerline of the roving projection, by determining the boundaries of R_i within the observation window W. Since rovings typically do not end within W only two boundaries should be present. To ensure this, boundaries shorter than 2.1 mm (300 voxels) were considered as artifacts and were removed. The two remaining boundaries,

which are roughly parallel, then were used to determine the orientation and position of the roving projection by averaging the orientations of both boundaries and computing their centroid.
Note that the resulting representation of each roving as a straight line in 2D, as shown in Figure 9a, is robust with respect to possible measurement artifacts. From this representation, we computed the intersection points of each pair of rovings.

3 Results

3.1 Image segmentation

Using the procedure stated in Section 2.3, an instance segmentation of individual rovings was computed, where the results are shown in Figure 4. More precisely, in Figure 4a, an in-plane slice of the CT-image is shown with normalized gray values, while Figure 4b shows the corresponding result of the 2.5D U-net segmentation. These results indicate a good distinction between the three phases, i.e., warp (orange), weft (blue), and matrix. Based on phase-wise segmentation, individual rovings were identified using a morphological erosion followed by a morphological dilation; see Section 2.3. An instance segmentation of the in-plane section is visualized in Figure 4c, while a 3D rendering of the instance segmentation is shown in Figure 4d. In total, 15 objects were obtained from which 13 rovings were identified in the image after ignoring very small objects with fewer than 100.000 voxels. For the remainder of the manuscript, the numbering of the rovings in Figure 4d is used to distinguish between rovings. In a last post-processing step, the curvature was corrected as discussed in Section 2.3.

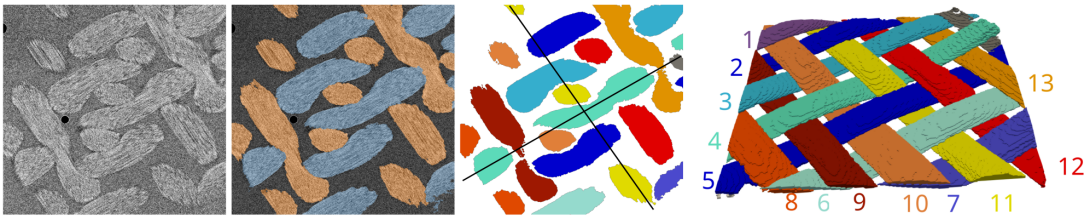

Figure 4: (a) in-plane section of a single layer (X-ray CT data), (b) phase-wise segmented in-plane section, (c) instance-wise segmented in-plane section, (d) instance-wise segmented single layer.

3.2 Cross section analysis along rovings

Based on the instance segmentation, the cross sections of each roving can be extracted. As shown in Figure 3 the cross sections vary along the length of the roving. These variations can be quantified by computing the geometrical descriptors introduced in Section 2.4 as functions of the y-position, i.e., the position along the roving. For consistency across rovings, we defined the zero coordinate of the y-position in the weft direction by the centerline of roving 4, while in the warp direction it is defined by the centerline of roving 11 (see the black lines in Figure 4c). This corresponds roughly to the center of the specimen in Section 2.1.
Figures 5 and 6 visualize the discussed descriptors for two exemplary rovings. Figure 5 shows the results for roving (10), orientated in warp direction, while Figure 6 presents roving (5), orientated in weft direction. The vertical bars mark the regions where the analyzed roving crosses other orthogonal rovings. More precisely, the intersection points are computed, and then a Gaussian filter [36] with $\sigma = 20$ is used to dilate these points. Note that, due to the periodic nature of the weave structure, the positions of orthogonal rovings are approximately evenly spaced.
In Figures 5a and 6a, the area of the cross sections along the roving is shown. In both cases, the area is between $0.18\,\mathrm{mm}^2$ and $0.26\,\mathrm{mm}^2$. Panels b and c show the lengths of the minor and major axes. Of these three descriptors, only the length of the minor axis exhibits a recognizable roughly periodic pattern for both rovings, while the cross sectional area exhibits a similar trend only for roving 5. The observed periodicity corresponds to intersections with orthogonal rovings, with maxima where the considered roving lies flat above or below orthogonal rovings and minima where it passes between orthogonal rovings.
Figures 5d and 6d show the z-position of the rovings, where positive and negative values imply that the considered roving is located above or below the orthogonal rovings, respectively. Together with the positions of the orthogonal rovings, as denoted by the vertical bars, the z-positions are characteristic for the considered 2/2 twill weave.
Similarly to the z-positions, the skewness and orientation as shown in Figures 5e,f, and 6e,f exhibit obvious periodic patterns. For both rovings considered, the skewness lies between -0.2 and 0.2. A negative skewness indicates that the roving is flatter at the bottom, while a positive skewness indicates that it is flatter at the top. Combining this information with the z-position, we can see that a positive skewness is observed if the roving is above the orthogonal rovings and a negative skewness is observed if it is under the orthogonal rovings. Moreover, the skewness is roughly 0, when passing between orthogonal rovings.
A correlation can also be observed for the orientation and the z-position. An orientation of 0° indicates that the roving is aligned parallel to the 2D plane. An orientation of $o(C_{i,j}) = 0$ occurs if the roving lies above or below two orthogonal rovings; see Figures 5f and 6f.
The three descriptors z-position, skewness, and orientation exhibit a sinusoidal progression with similar wavelengths. Thus, we fitted sinusoidal curves to each of these descriptors as explained in Section 2.4. Recall the common definition of the zero

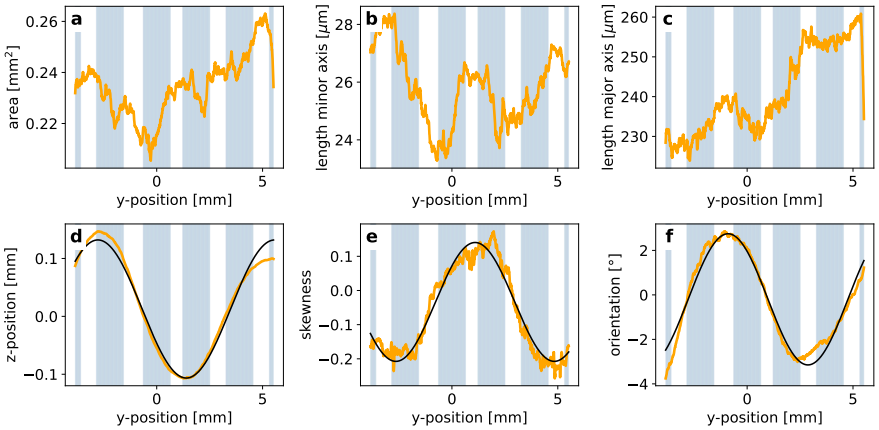

Figure 5: z-position (left), skewness (middle) and orientation (right) of the cross section of a selected roving (10) at different longitudinal positions (y) with fitted sinus function. Vertical blue bars mark regions where the roving crosses other rovings, clearly showing the 2/2 twill weave.

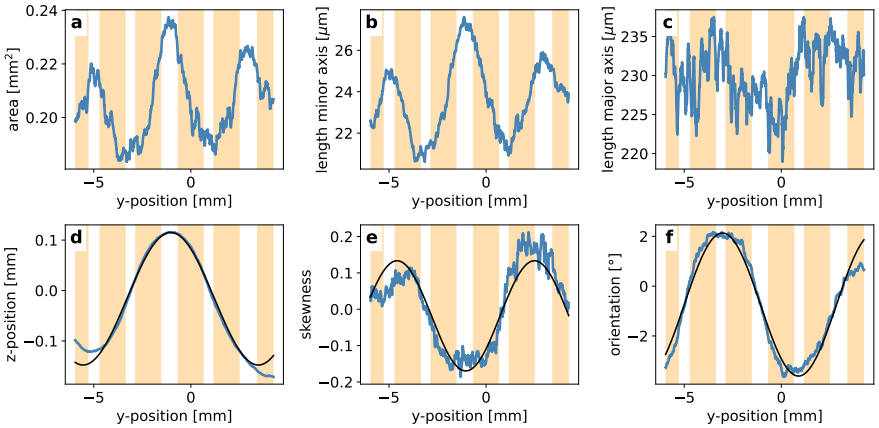

Figure 6: z-position (left), skewness (middle) and orientation (right) of the cross section of a selected roving (5) at different longitudinal positions (y) with fitted sinus function. Vertical orange bars mark regions where the roving crosses other rovings, clearly showing the 2/2 twill weave.

coordinate of the y-position which is used to define the phase of the curves. Note that we only consider rovings with a length of at least 3.5 mm to ensure that the sinusoidal curve is recognizable. The resulting parameters of the sinusoidal curve of Eq. (1) are given in Table 1. In the following, we consider the wavelength $\omega = 2\pi/f$ for better interpretability.

Table 1: Estimated sinusoidal parameters (wavelength $\omega = 2\pi/f$) for each roving and each geometrical descriptors z-position, skewness, and orientation. Colors indicate the roving direction: blue for weft and orange for warp. (par. = parameter).

descriptor	par.	R_2	R_3	R_4	R_5	R_6	R_7	R_9	R_{10}	R_{11}	R_{12}	R_{13}
z-position	A	0.16	0.10	0.13	0.13	0.13	0.16	0.11	0.12	0.16	0.11	0.13
	ω [mm]	8.53	7.92	8.43	9.03	8.58	10.55	7.85	8.35	8.90	8.15	11.55
	Φ [mm]	0.90	5.61	3.86	2.29	0.59	5.27	5.60	3.66	2.48	0.85	5.30
	C	−0.02	0.03	0.01	−0.02	−0.01	0.05	0.00	0.01	0.01	0.01	0.01
skewness	A	0.18	0.15	0.16	0.15	0.11	0.24	0.19	0.17	0.25	0.29	0.19
	ω [mm]	6.20	8.49	7.67	7.07	6.62	9.73	8.09	7.48	8.06	7.75	14.78
	Φ [mm]	4.04	2.16	0.92	5.64	4.06	3.31	2.38	0.65	5.69	3.84	3.17
	C	−0.05	−0.02	−0.02	−0.02	0.05	0.00	0.00	−0.03	−0.01	−0.03	−0.04
orientation	A	132.96	2.22	3.69	2.87	2.47	7.19	3.41	2.95	3.40	3.06	9410.31
	ω [mm]	65.03	8.08	9.25	7.84	6.18	8.67	8.25	7.54	8.18	7.48	482.19
	Φ [mm]	1.71	0.90	5.33	4.00	2.91	1.53	4.07	2.32	0.84	5.99	4.71
	C	−126.15	0.78	−0.45	−0.74	0.63	−1.94	0.02	−0.20	0.04	0.56	9408.49

Considering the cross sectional orientation, the wavelengths of the rovings R_2 and R_{13} are 65.03 and 482.19, respectively. However, in all other cases the wavelength is between 6.18 and 14.78. Thus, the wavelengths of 65.03 and 482.19 appear to be

outliers, caused by the relatively short portions of the rovings R_2 and R_{13} captured in the scan. In addition, for all other rovings, the wavelength deviation for the three descriptors is at most 2.4. Thus, it can be observed that the sinusoidal curves of the three descriptors have similar wavelengths for the most descriptors.
To further analyze the relation between the z-position, the skewness, and the orientation, the phase difference is calculated for all of them in degree by

$$\Delta\Phi^i_{d_1,d_2} = min\{|\Phi^i_{d_1} - \Phi^i_{d_2}|, 2\pi - |\Phi^i_{d_1} - \Phi^i_{d_2}|\} \cdot \frac{180}{\pi}, \tag{3}$$

where $d_1, d_2 \in \{\text{z-position,skewness,orientation}\}$ and $i \in \{2,3,4,5,6,7,9,10,11,12,13\}$. The phase of the descriptors d_1, d_2 of the i-th roving is denoted by $\Phi^i_{d_1}$ and $\Phi^i_{d_2}$, respectively. For example, a phase difference of 180° means that the sinusoidal curve of d_1 has a minimum when the sinusoidal curve of d_2 has a maximum. The results are shown in Figure 7.

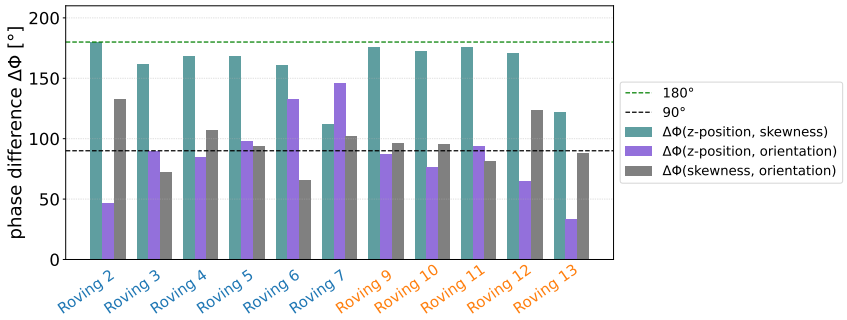

Figure 7: Phase difference of z-position, skewness and orientation for warp rovings (orange) and weft rovings (blue).

The skewness tends to be phase shifted by 180° compared to the z-position. More precisely, the phase shift is between 160° and 180° for all rovings except for R_7 and R_{13}. The phase difference between orientation and z-position is between 75° and 105° for $R_3, R_4, R_5, R_9, R_{10}$ and R_{11}. Recall that the sinusoidal fits for the cross sectional orientation of R_2 and R_{13} seem to be outliers.
In addition, the error between the true descriptor values and the corresponding values predicted by fitting the sinusoidal curve is shown in Figure 8. In general, no significant differences are observed between the two directions, with small errors for all three descriptors. As can be seen in Figures 5d,f and 6d,f, errors in orientation and z-position occur mainly near the edge of the sample. Since skewness involves more fluctuations along the entire roving, errors are evenly distributed across the entire roving.

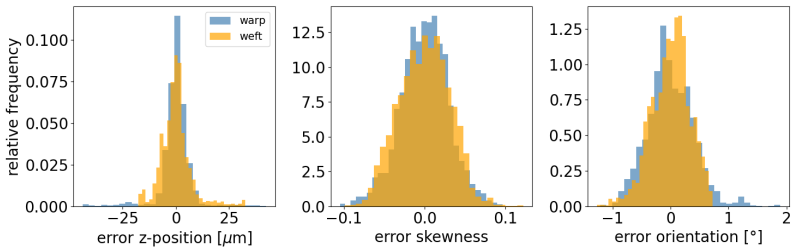

Figure 8: Histograms of the errors between the true descriptor values and the corresponding values predicted by the fitted sinusoidal curve, shown for all rovings in both directions. Left: z-position, middle: skewness, right: orientation.

3.3 Analysis of the weave structure

To analyze the weave structure, the centerlines of the rovings were used, see Section 2.4. Based on these centerlines, the intersection points are determined. The resulting grid of the centerlines with the corresponding roving orientations is shown in Figure 9a.
It is noticeable that there is an outlier in the warp direction with respect to the orientation at the edge with 55.8°, while the other values lie between 59.7° and 59.9°. A greater variability in terms of orientation can be observed for the weft direction. Here, the values are distributed between −32.2° and −34.4°. In addition, the distances between two intersection points along the rovings in different directions are analyzed and shown in Figure 9b. Due to the variations in roving orientation, some variations in the distance between the intersection points are expected. More precisely, the standard deviations are 0.18 mm and 0.14 mm for the weft and warp directions, while the mean is 2.02 mm for both directions. Thus, some irregularities can be observed, especially in the weft direction.

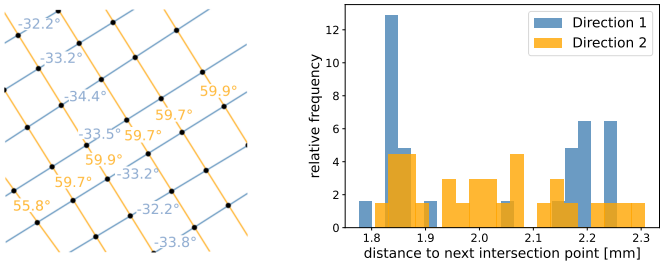

(a) (b)

Figure 9: Centerlines of the rovings with corresponding orientation (a) and histograms of the relative frequency of the distances between two intersection points in warp (orange) and weft (blue).

4 Discussion

In order to better evaluate the results, it is necessary to consider how and to what extent the individual geometric descriptors are influenced by segmentation and post-processing. For example, the quality of the instance segmentation directly influences the analysis of the rovings and the weave structure. Recall that in a first step, a phase-wise segmentation based on U-net was performed, providing good results which lead to a reasonable division into warp, weft and matrix, see Figure 4. Afterward, a morphological erosion with radius $r = 5.0$ followed by a dilation with $r = 4.9$ is performed to obtain the instance segmentation. Due to the chosen radii, boundary effects are possible. More precisely, there may be some small loss at the edges of the rovings, as can be seen in Figure 4c. However, using a smaller radius or the same radius for the morphological erosion and subsequent dilation does not lead to a complete separation of all rovings. Although some boundary effects may still occur, the overall segmentation results remain satisfactory. Furthermore, it should be taken into account that the z-position, the skewness, and the orientation are relatively stable against small segmentation errors, while the area and the length of the minor and major axes are more sensitive. Moreover, the analysis of the weave structure is stable with respect to some boundary effects of the segmentation. In addition, a slight curvature caused by sample preparation was observed for the specimen. This would have an influence on the geometrical descriptors, especially on the orientation of the cross sections. Therefore, it was corrected on the basis of a cubic polynomial, which corrects the systematic error. Although this correction is applied only in the through-plane direction, the resulting structural distortion is minimal and negligible due to the absence of strong curvature.

The scanned rovings showed some limited splaying at a few roving ends, which is consistent with edge effects typically introduced at the physical boundaries of punched specimens where the weave pattern becomes disrupted. In fact, the scanned region originated from the central part of the specimen. Figure 1 confirms this, revealing approximately 11 rovings in each direction and placing the expected geometric center of the sample in the vicinity of rovings 3, 4, 11, and 12. However, it should be noted that the specimen consists of a single fabric layer and is inherently flexible before embedding (e.g., drapability during handling or processing), which can lead to slight geometric changes. Such deformation effects cannot be entirely excluded, even under careful handling. Taking all these aspects into account, it nevertheless becomes clear that the cross sections significantly vary along rovings. This can be seen for all geometric descriptors. Especially in Figure 6 a, b, d, and e a periodic variation and inter-connectivity of the area, length minor axis, z-position, skewness and orientation can be observed. The periodic variation is less pronounced for the area and length of the minor axis; see Figure 5. Nevertheless, there appears to be a correlation such that the area and length of the minor axis have a lower value when the roving runs through two orthogonal rovings compared to when it lies on or below two orthogonal rovings. Since the number of fibers within a roving is constant, the fiber volume content along the roving can be determined directly through the area. For roving 10 and 5 in Figure 5 and Figure 6, the fiber volume content varies from 44% to 52% and 47% to 53%, respectively. This difference in the intra-tow fiber volume leads to differences in the pore space on the microscale, which would then influence the impregnation of the tow fibers or may affect microscale damage mechanisms. While this consideration assumes that the fiber structure was present prior to impregnation and acknowledges possible tow rearrangement during resin flow, the observed differences may still offer valuable insights into processing-related phenomena.

The periodic changes were most pronounced for z-position, skewness, and orientation. Thus, a sinusoidal curve was fitted to further analyze these periodic changes. The use of periodic functions to describe the geometric oscillation in woven textiles is fundamentally justified, as the architecture of woven structures is inherently periodic. In the case of a 2/2 twill weave, where each roving undergoes an equal number of over- and under-crossings, a sinusoidal function represents a reasonable and mathematically well-behaved approximation of the roving trajectory; see Figure 8. In addition, the approximation of the skewness and orientation of the roving cross section leads to minor errors. However, there are two outliers in the sinusoidal curve fit, i.e., for the orientation of R_2 and R_{13}, which leads to an unrealistic progression if one considers the subsequent course of the sinus. Only small portions of these two rovings are captured in the image data. Thus, a larger image section would probably lead to a more realistic sinusoidal curve.

Still, the remaining sinusoidal curve fits can be used to further analyze the relation between the geometrical descriptors based on

the phase shifts. Skewness is usually phase shifted by 180°. Thus, the cross section is flatter at the bottom when the roving lies above two orthogonal rovings and flatter at the top when the roving lies below two orthogonal rovings. The most likely reason for this is that normal contact stresses at the crossing result in a rearrangement of the fibers within the roving, leading to local compaction and flattening on the contacting side before the infusion of epoxy resin. This effect is further enhanced by the tension during weaving or placement, which increases the normal stress and limits the roving's ability to return to its original shape. Although this phenomenon has been reported frequently in the literature; see [21, 37], it is rarely incorporated into stochastic models. Skewness provides a way to quantify this effect and thereby facilitates its integration into a stochastic model. In addition, the cross sectional orientation is usually phase shifted by 90°. Thus, the cross section is aligned horizontally when the roving lies below or over two orthogonal rovings.

It is important to emphasize that skewness and cross sectional orientation do not merely describe the shape of the rovings but may directly influence the actual fiber trajectories inside the rovings. The regions analyzed correspond to the interior of the fiber bundles, i.e., the domains in which the carbon fiber filaments reside. A periodic rotation of the cross section may indicate that the fibers inside the roving experience a slight lateral redistribution, which means that their local alignment could deviate from the nominal roving path.

In addition, the weave structure is analyzed. As can be seen in Figure 9, some irregularities can be observed in the roving trajectories. The roving orientation is relatively stable for the rovings in the weft direction. Some larger variations can be observed in the warp direction. The observed irregularities could be induced by the weaving process: During the fabric production, the warp rovings are moved up and down to the shed through which the weft rovings are guided. This repeated motion may subject the warp system to mechanical loading different from that of the weft rovings, which could contribute to slight differences in the resulting roving geometries between both directions.

In general, some irregularities can be observed in the laminate based on geometrical descriptors. These irregularities influence the mechanical properties of the material [15, 16]. Thus, a stochastic microstructure model should be able to display such variations. The observed periodic variation can be used to model the roving cross sections. Although the purely sinusoidal representation worked well for the presented 2/2 twill case, it should be noted that this may not necessarily hold for weave patterns with more transitions or for satin weaves, where the roving path can deviate more strongly from a simple first-harmonic shape. However, the approach could be extended by incorporating additional harmonics through a Fourier series. This would allow sharper transitions and asymmetric features—such as local flattening or non-ideal roving bending—to be represented more accurately.

5 Conclusions

In this work, the µ-CT image of a single layer CFRP laminate, consisting of a 2/2 twill, was analyzed. Therefore, an instance segmentation was performed using a 2.5D U-net with subsequent morphological erosion and dilation. Then, various geometric descriptors, i.e., length of minor and major axes, z-position, skewness, and orientation, were computed for the roving cross sections. For z-position, skewness and orientation a periodic progression was observed along the rovings, which can be modeled by sinusoidal curves.The descriptors considered examine the variations in the cross-section along the rovings very precisely. This enables very realistic stochastic structural modeling of the cross-section along the rovings. It is also observed that the weave structures show some variation, especially the roving orientation in weft direction. Thus, it is observed that the roving cross sections and the weave structures show some variation within the laminate. These variations should be displayed in a 3D microstructure model, since they influence material properties. Consequently, the results of this work can be used as a preliminary work for a realistic stochastic 3D microstructure model. Such a stochastic model enables the simulation of synthetic laminates, which can then be used to make predictions about material properties using numerical simulations.

References

[1] E. Syerko, T. Schmidt, D. May, C. Binetruy, S. Advani, S. Lomov, L. Silva, S. Abaimov, N. Aissa, I. Akhatov, M. Ali, N. Asiaban, G. Broggi, J. Bruchon, B. Caglar, H. Digonnet, J. Dittmann, S. Drapier, A. Endruweit, A. Guilloux, R. Kandinskii, A. Leygue, B. Mahato, P. Martínez-Lera, M. Matveev, V. Michaud, P. Middendorf, N. Moulin, L. Orgéas, C. Park, S. Rief, M. Rouhi, I. Sergeichev, M. Shakoor, O. Shishkina, Y. Swolfs, M. Tahani, R. Umer, K. Vanclooster, R. Vorobyev, Benchmark exercise on image-based permeability determination of engineering textiles: Microscale predictions, Composites Part A: Applied Science and Manufacturing 167 (2023) 107397.

[2] S. R. Stock, Recent advances in X-ray microtomography applied to materials, International Materials Reviews 53 (2008) 129–181.

[3] A. V. Bronnikov, Phase-contrast CT: Fundamental theorem and fast image reconstruction algorithms, SPIE, 2006, p. 63180Q.

[4] F. Pfeiffer, T. Weitkamp, O. Bunk, C. David, Phase retrieval and differential phase-contrast imaging with low-brilliance x-ray sources, Nature Physics 2 (2006) 258–261.

[5] J. Kastner, B. Plank, C. Gusenbauer, S. Senck, A. Sasov, Talbot-Lau grating interferometer X-ray computed tomography for the characterization of fiber-reinforced polymers, Digital Industrial Radiology and Computed Tomography 20 (2015) 22–25.

[6] J. Kim, M. Kagias, F. Marone, M. Stampanoni, X-ray scattering tensor tomography with circular gratings, Applied Physics Letters 116 (2020) 134102.
[7] M. Kagias, Z. Wang, M. E. Birkbak, E. Lauridsen, M. Abis, G. Lovric, K. Jefimovs, M. Stampanoni, Diffractive small angle X-ray scattering imaging for anisotropic structures, Nature Communications 10 (2019) 5130.
[8] I. Straumit, S. V. Lomov, M. Wevers, Quantification of the internal structure and automatic generation of voxel models of textile composites from X-ray computed tomography data, Composites Part A: Applied Science and Manufacturing 69 (2015) 150–158.
[9] S. V. Lomov, R. Parnas, S. Bandyopadhyay Ghosh, I. Verpoest, A. Nakai, Experimental and theoretical characterization of the geometry of two-dimensional braided fabrics, Textile Research Journal 72 (2002) 706–712.
[10] Y. Sinchuk, P. Kibleur, J. Aelterman, M. Boone, W. Van Paepegem, Variational and deep learning segmentation of very-low-contrast X-ray computed tomography images of carbon/epoxy woven composites, Materials 13 (2020) 936.
[11] B. Boos, K.-C. Chen, A. Gebhard, M. Gurka, Segmentation of a CFRP weave structure for material characterization and simulation, e-Journal of Nondestructive Testing 30 (2025). doi:https://doi.org/10.58286/30714.
[12] S. Garcea, Y. Wang, P. Withers, X-ray computed tomography of polymer composites, Composites Science and Technology 156 (2018) 305–319.
[13] B. Boos, C. Queck, M. Gurka, High resolution – large field-of-view 3D imaging of fiber-reinforced composites with complex microstructure: stitching of lab-CT scans with single fiber resolution, Methods in Microscopy 2 (2025) 303–305.
[14] M. Weber, A. Grießer, D. Mosbach, E. Glatt, A. Wiegmann, V. Schmidt, Investigating microstructure–property relationships of nonwovens by model-based virtual material testing, Transport in Porous Media 151 (2024) 1403–1421.
[15] S. Green, M. Matveev, A. Long, D. Ivanov, S. Hallett, Mechanical modelling of 3d woven composites considering realistic unit cell geometry, Composite Structures 118 (2014) 284–293.
[16] G. Balokas, B. Kriegesmann, S. Czichon, R. Rolfes, Stochastic modeling techniques for textile yarn distortion and waviness with 1d random fields, Composites Part A: Applied Science and Manufacturing 127 (2019) 105639.
[17] S. Blusseau, Y. Wielhorski, Z. Haddad, S. Velasco-Forero, Instance segmentation of 3D woven fabric from tomography images by Deep Learning and morphological pseudo-labeling, Composites Part B: Engineering 247 (2022) 110333.
[18] M. Sherburn, Geometric and Mechanical Modelling of Textiles, PhD thesis, University of Nottingham (July 2007).
[19] H. Wang, Z.-W. Wang, A variable metric stochastic theory of textile composites with random geometric parameters of yarn cross-section, Composite Structures 126 (2015) 78–88.
[20] F. Gommer, L. Brown, K. Wedgwood, Analytical method using gamma functions for determining areas of power elliptical shapes for use in geometrical textile models, Composites Part A: Applied Science and Manufacturing 81 (2016) 222–224.
[21] R. Sevenois, D. Garoz, F. Gilabert, S. Spronk, S. Fonteyn, M. Heyndrickx, L. Pyl, D. Van Hemelrijck, J. Degrieck, W. Van Paepegem, Avoiding interpenetrations and the importance of nesting in analytic geometry construction for representative unit cells of woven composite laminates, Composites Science and Technology 136 (2016) 119–132.
[22] Math2Market GmbH, GeoDict 2025 User Guide, Germany (2025). doi:10.30423/userguide.geodict.
[23] H. Lin, L. Brown, A. Long, Modelling and simulating textile structures using texgen, Advanced Materials Research 331 (2011) 44–47.
[24] I. Verpoest, S. V. Lomov, Virtual textile composites software WiseTex: Integration with micro-mechanical, permeability and structural analysis, Composites Science and Technology 65 (2005) 2563–2574.
[25] B. Ozgen, H. Gong, Yarn geometry in woven fabrics, Textile Research Journal 81 (2011) 738–745.
[26] Dragonfly 2024.1, Comet Technologies Canada Inc., Montreal, Canada, https://dragonfly.comet.tech.
[27] P. Soille, Morphological Image Analysis: Principles and Applications, Springer, 2004.
[28] R. Gong, B. Ozgen, M. Soleimani, Modeling of yarn cross-section in plain woven fabric, Textile Research Journal 79 (2009) 1014–1020.
[29] S. N. Chiu, D. Stoyan, W. S. Kendall, J. Mecke, Stochastic Geometry and its Applications, 3rd Edition, J. Wiley & Sons, 2013.
[30] W. K. Pratt, Introduction to Digital Image Processing, CRC Press, 2013.
[31] S. Lomov, G. Huysmans, Y. Luo, R. Parnas, A. Prodromou, I. Verpoest, F. Phelan, Textile composites: modelling strategies, Composites Part A: Applied Science and Manufacturing 32 (2001) 1379–1394.
[32] Y. Zhou, W. Wen, H. Cui, Spatial modelling of 3D woven variable thickness composite plate at the mesoscopic scale, Composite Structures 239 (2020) 111946.
[33] G. Hivet, P. Boisse, Consistent 3D geometrical model of fabric elementary cell. Application to a meshing preprocessor for 3D finite element analysis, Finite Elements in Analysis and Design 42 (2005) 25–49.
[34] Y. Zhou, H. Cui, J. Chen, Geometric modeling of 3D woven composite tube RVE with cross-section variations, Fibers and Polymers 25 (2024) 3945–3956.
[35] F. Pedregosa, G. Varoquaux, A. Gramfort, V. Michel, B. Thirion, O. Grisel, M. Blondel, P. Prettenhofer, R. Weiss, V. Dubourg, J. Vanderplas, A. Passos, D. Cournapeau, M. Brucher, M. Perrot, E. Duchesnay, Scikit-learn: Machine learning in Python, Journal of Machine Learning Research 12 (2011) 2825–2830.

[36] E. Cuevas, A. N. Rodríguez, Image Processing and Machine Learning, Volume 1: Foundations of Image Processing, Chapman and Hall/CRC, 2024.
[37] Z. Yousaf, P. Withers, P. Potluri, Compaction, nesting and image based permeability analysis of multi-layer dry preforms by computed tomography (CT), Composite Structures 263 (2021) 113676.